Ocean Dynamics (2014) 64:999–1018
DOI 10.1007/s10236-014-0725-6

Marine radar ocean wave retrieval's dependency on range and azimuth

Björn Lund · Clarence O. Collins · Hans C. Graber · Eric Terrill · Thomas H. C. Herbers

Received: 22 January 2014 / Accepted: 17 April 2014 / Published online: 14 June 2014

Abstract The strength of the surface wave signal in marine X-band radar (MR) images strongly depends on range and azimuth (i.e., the angle between antenna look and peak wave direction). Traditionally, MR wave analysis is carried out in a set of rectangular windows covering the radar field of view (FOV). The FOV is typically partially obstructed, e.g., due to the coastline or ship superstructures. Especially for ships that are subject to regular course changes, this results in an increased variability or error associated with wave parameters. Using MR measurements from R/P FLIP, acquired off California during the 2010 US Office of Naval Research (ONR) high resolution air–sea interaction (Hi-Res) experiment, this study quantifies the dependency of the radar-based 2D wave spectrum and parameters on range and azimuth. With the help of reference data from a nearby Datawell Waverider buoy, we propose empirical methods to remove the dependency and we illustrate their efficacy.

Responsible Editor: Val Swail

This work has been supported by the US Office of Naval Research under grants N000140710650, N000140810793, N000140910392, and N000141310288.

This article is part of the Topical Collection on the *13th International Workshop on Wave Hindcasting and Forecasting in Banff, Alberta, Canada October 27 - November 1, 2013*

B. Lund (✉) · H. C. Graber · C. O. Collins
Rosenstiel School of Marine and Atmospheric Science, University of Miami, 4600 Rickenbacker Causeway, Miami, FL, 33149 USA
e-mail: blund@rsmas.miami.edu

E. Terrill
Scripps Institution of Oceanography, University of California, San Diego, La Jolla, CA, USA

T. H. C. Herbers
Naval Postgraduate School, Monterey, CA, USA

Keywords Ocean waves · Shipboard wave measurements · Marine X-band radar · Remote sensing

1 Introduction

Surface waves influence the exchange of mass, momentum, and energy between the atmosphere and the ocean. Wave measurements therefore play an important role for air–sea interaction studies (e.g., Donelan et al. 1997). Numerous ocean wave processes and properties remain poorly understood, for example, deep-water wave breaking or the wave spectrum's shape in the equilibrium range (Thomson et al. 2013). Knowledge of the surface waves (and currents) is also required for evaluating sea loads and motions acting on ships and offshore structures. Access to real-time directional wave spectra can aid navigation and improve operational safety on ships(e.g., Nielsen et al. 2006). While the various existing wave sensors tend to agree well on peak wave parameters, they compare less favorably regarding the wave field's directional characteristics and the low-energy sections of the wave frequency spectrum (Collins et al. 2013). On ships, the platform motion presents an additional challenge for wave measurements. This paper aims at improving marine X-band radar (MR) ocean wave measurements from both fixed and moving platforms by quantifying and removing the wave retrieval's dependency on range and azimuth.

MRs operate by transmitting and receiving pulses of microwaves at grazing incidence, typically with horizontal polarization on send and receive (HH). The radar pulses interact with the centimeter-scale sea surface roughness through Bragg scattering (Plant and Keller 1990). The long surface waves' orbital motion modulates the radar-scattering elements (Alpers et al. 1981). In addition, the

long waves modify the radar backscatter by changing the effective local incidence angle and by partially shadowing the sea surface (Wetzel 1990). Finally, micro-breakers that are concentrated near the long-wave crests are believed to contribute significantly to the backscatter, especially for HH (Lee et al. 1995). The combination of these radar backscatter modulation mechanisms leads to the so-called *sea clutter* in MR images, alternating regions of dark and bright backscatter, in-phase with the surface waves. This ocean wave footprint within MR backscatter measurements, combined with MR's capability of scanning the sea surface with a high spatio-temporal resolution, explains why MRs have great potential for sea state monitoring.

Since MRs were developed for ship detection, however, sea clutter was first discussed as a source of noise that may obscure small target echoes (e.g., Croney et al. 1966). But once (Young et al. 1985) introduced a fast Fourier transform (FFT)-based analysis technique to determine directional ocean wave spectra from MR image sequences, MRs have become a popular surface wave retrieval instrument, with commercial products being offered by OceanWaveS and MIROS, among others. Today, MR sea clutter has been exploited in numerous oceanographic studies with a variety of topics, including surface waves (Hessner et al. 2001; Borge and Soares 2000), surface currents (Senet et al. 2001), bathymetry (Bell 1999), surface elevation maps (Borge et al. 2004), wind vectors (Dankert and Horstmann 2007; Lund et al. 2012b), wave breaking (Catalán et al. 2011), and internal waves (Ramos et al. 2009; Lund et al. 2013).

Most MR wave studies discussed in the literature were based on data from coastal stations, e.g., light houses, or offshore platforms (Wyatt et al. 2003; Hessner et al. 2008; Reichert and Lund 2007). While these studies generally find good agreement between MR and reference wave measurements, recent publications suggest that shipboard wave radars lag behind their fixed-platform cousins in terms of performance. (Stredulinsky and Thornhill 2011) show that while radar-based direction and frequency measurements from moving vessels are good, significant wave height H_s estimates are unreliable. They propose a shipboard wave measurement technique that combines radar data with measured ship motion response data. This sensor fusion approach was adapted by Cifuentes-Lorenzen et al. (2013) who use a laser altimeter to scale the radar-based wave spectra. In their comparison of multiple shipboard wave sensors, they find that discrepancies increase with ship speed. In particular, measurements are found to be adequate at ship speeds of 3 ms^{-1} or less, but fail at speeds above 5 ms^{-1}. Note that both aforementioned studies obtained their shipboard MR surface wave results using a commercial Wave Monitoring System (WaMoS) that employs the exact same analysis techniques as for fixed platforms, the only exception being that the system includes the mean horizontal ship motion, treating it as a virtual current (Ziemer 1995). (Serafino et al. 2011) propose a simple georeferencing technique to mitigate the ship motion-induced aliasing effect. (Ludeno et al. 2013) applied this technique to MR data from a cruise ship and found good agreement with modeling results. However, their discussion hardly touches on H_s, the parameter that is arguably the most difficult to determine using shipboard (and fixed platform) MR.

One important source of error has been widely neglected in the literature: The strength of the surface wave signal in MR images strongly depends on range (i.e., the distance from the radar antenna) and azimuth (the angle between antenna look and peak wave direction). Especially for ships that are subject to regular course changes, this dependency leads to an increased error associated with wave parameters. This paper focuses on the dependency of the MR wave results on range and azimuth. The azimuth dependency of MR surface wave estimates was first investigated by Reichert (1994). Ideally, this issue could be addressed by using multiple analysis windows that are distributed evenly over the whole image, covering all directions. However, on most MR installations, this is not possible because the radar field of view (FOV) is partially obstructed, e.g., by ship superstructures. The goal of this paper is to quantify how the MR wave spectra change with range and azimuth. Based on our findings, we propose a new correction technique that we believe will significantly improve MR wave estimates, especially for shipboard applications. We therefore hope that this study will contribute to wave science, aid offshore engineering, and enhance safety on ships.

This paper is organized as follows: Section 2 gives an overview of our data. The MR surface wave retrieval technique is revisited in Section 3. In Section 4, we present and discuss the results from our analysis of the wave retrieval's dependency on range and azimuth. Section 5 draws conclusions and provides an outlook for future work.

2 Data overview

In this study, we analyze MR data that were collected from R/P FLIP during US Office of Naval Research (ONR)'s high resolution air–sea interaction (Hi-Res) experiment in June 2010. The Hi-Res experiment took place on the continental shelf off the coast of California, where FLoating Instrument Platform (FLIP) was moored in a water depth of 165 m. A map of the area with FLIP's location and bathymetric information is shown in Fig. 1. The broad goal of Hi-Res was to determine and predict the phase-resolved surface wave field. One particular goal of the project was to evaluate MRs' ability to measure individual waves. A standard Furuno MR was therefore installed on FLIP. (Another MR was installed on R/V Sproul that was deployed to take additional

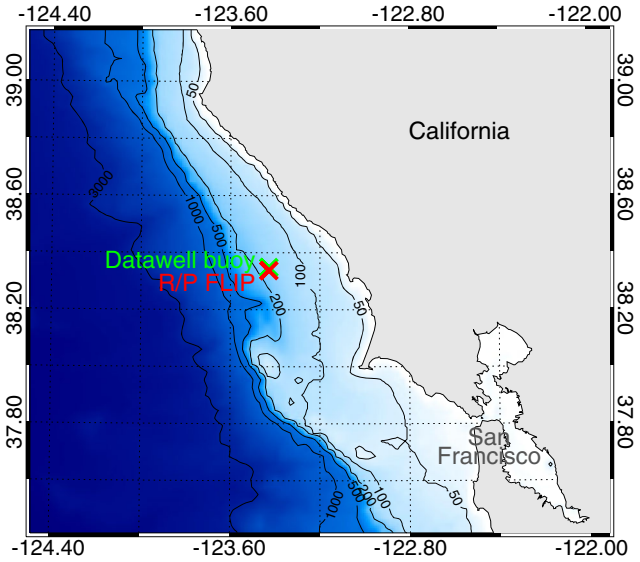

Fig. 1 Map with locations of FLIP and Datawell buoy during Hi-Res 2010. The bathymetry was extracted from the GEBCO Digital Atlas published by the British Oceanographic Data Centre

measurements during part of the experiment.) FLIP (FLoating Instrument Platform) is a 108-m long non-propelled manned research platform that is towed in the horizontal position to its operating area and then, through ballast changes, flipped to the vertical position. Once upright, with ∼ 91 m submerged under water, FLIP becomes a relatively stable spar buoy, ideal for air–sea interaction studies. Figure 2 shows a picture of FLIP in its upright position.

The MR on FLIP was connected to OceanWaveS' WaMoS radar data acquisition board. WaMoS consists of an analog-to-digital converter, a personal computer for data storage and analysis, and a screen to display results. Figure 3 shows a diagram of the WaMoS hardware. The radar was

Fig. 2 Picture of FLIP in its upright position. Source: http://www.ucsd.edu

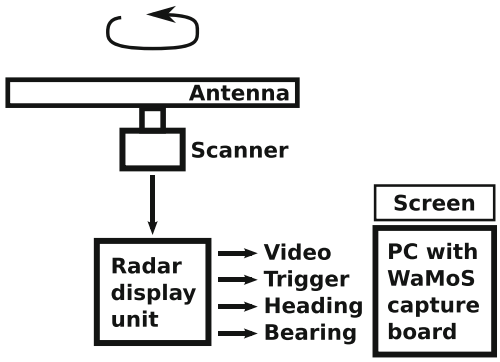

Fig. 3 WaMoS hardware components

operating at 9.4 GHz (X-band) with HH polarization and grazing incidence angle. The 8-foot long antenna has a horizontal beam width of 0.75°, a rotation rate of 40 rpm, and was installed at a height of ∼ 30 m. The radar was set to operate at short pulse mode (i.e., a pulse length of 0.07 ∝s), which results in a range resolution of 10.5 m. Since the MR range and azimuth resolution depend on the radar pulse and antenna length, respectively, the accuracy of the MR wave estimates can be expected to improve as the pulse length is shortened and the antenna length increased. WaMoS was set to collect images over a range from 120 to 3,960 m with a grid size of 7.5 m in range and ∼ 0.25° in azimuth. The system stores the logarithmically amplified radar backscatter information at 12-bit image depth, i.e., digitized backscatter intensities range from 0 to 4,095. As is typical for conventional MRs, the measured backscatter intensities were not radiometrically calibrated.

The MR data were complemented by in situ wave measurements from a Datawell DWR-G7 Directional Waverider Buoy that was deployed near FLIP, 157 m above the seafloor. The position of the Datawell buoy is marked in Fig. 1. The buoy sampled horizontal (north, west) and vertical displacements continuously at 1.28 Hz. The buoy data were processed in hour-long records using standard techniques to estimate the surface height spectrum, mean direction as a function of frequency, and directional spread as a function of frequency, as well as bulk parameters (O'Reilly et al. 1996).

3 Review of marine radar surface wave retrieval

This section revisits the well-established FFT-based technique to retrieve wave spectra (and surface currents) from 3D MR backscatter data. For a more in-depth discussion, the reader is referred to Senet et al. (2001), Borge et al. (2004), and Borge et al. (2008). As mentioned in Section 1, the radar backscatter from the sea surface is a complicated process

that is dominated by hydrodynamic modulation, tilt modulation, and shadowing. Furthermore, the radar backscatter intensity decays rapidly with range and strongly depends on the wind (Dankert and Horstmann 2007; Lund et al. 2012b). It should therefore be clear that the radar backscatter intensities do not scale linearly with the sea surface elevation.

Figure 4 illustrates the MR backscatter data acquisition for two consecutive antenna rotations. The continuously rotating radar antenna repeatedly transmits microwave pulses and receives their backscatter from the sea surface. In a space-time cube, the MR backscatter data therefore resembles a spiral staircase. For practical reasons, however, it is typically assumed that the radar backscatter recorded during each antenna rotation represents a spatio-temporal snapshot of the sea surface (e.g., Borge et al. 1999; Senet et al. 2001; Bell and Osler 2011). Figure 5 gives an example of one such "snapshot" acquired from a research vessel where a 50° wide section of the radar FOV towards the stern was blocked by superstructures. The sea clutter is clearly visible, with the dominant waves approaching the ship at a slight port-side angle (from west–northwest). The wave analysis is typically carried out in a set of rectangular windows that cover the sea surface area illuminated by the radar (OceanWaveS GmbH 2012). The analysis windows shown in the figure are approximately 2 km^2 in size.

Let us assume sea state is a linear, zero-mean, Gaussian process that is homogeneous in space $\mathbf{r} = (x, y)$ and stationary in time t. Under these assumptions, the surface elevation can be written as a superposition of plane waves

$$\eta(\mathbf{r}, t) = \int_{\Omega_{\mathbf{k},\omega}} \exp[i(\mathbf{k}\cdot\mathbf{r} - \omega t)]\mathrm{d}Z(\mathbf{k}, \omega) + \text{c.c.} \qquad (1)$$

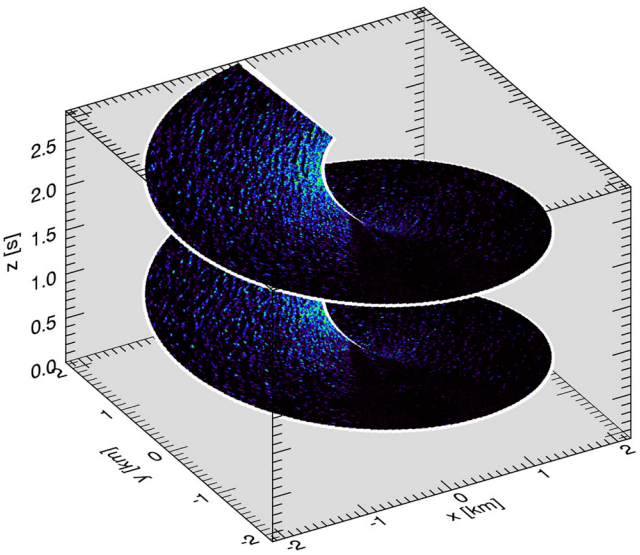

Fig. 4 MR backscatter data acquisition spiral covering two antenna rotations

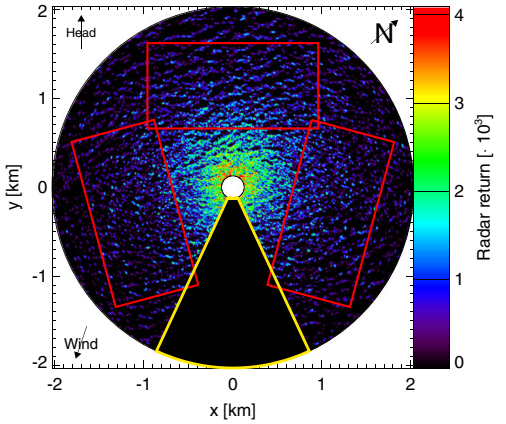

Fig. 5 Single radar image with example rectangular wave analysis windows in *red* and a blacked-out section with *yellow frame* where the radar FOV is obstructed

where $\mathbf{k} = (k_x, k_y)$ is the wave number, ω is the angular frequency, $\mathrm{d}Z(\mathbf{k}, \omega)$ is the random complex amplitude, and c.c. stands for the complex conjugate. The integration domain $\Omega_{\mathbf{k},\omega}$ is defined as the admissible range of wave numbers and frequencies for swell and wind sea (Komen et al. 1996). In practice, the integration domain is limited by the measuring sensor's spatial and temporal sampling resolutions. The 3D wave spectrum is defined as

$$F_W(\mathbf{k}, \omega)\mathrm{d}^2\mathbf{k}\mathrm{d}\omega = \epsilon[\mathrm{d}Z(\mathbf{k}, \omega)\mathrm{d}Z^*(\mathbf{k}, \omega)] \qquad (2)$$

where ϵ is the expectation operator, and the superscript * indicates the complex conjugate (Borge et al. 2008).

As a first order approximation, we can further assume that surface waves follow the dispersion relationship

$$\omega = \pm\sqrt{gk\tanh kh} + \mathbf{k}\cdot\mathbf{U} \qquad (3)$$

where $k = |\mathbf{k}|$, g is the acceleration due to gravity, h is the water depth, and $\mathbf{U} = (U_x, U_y)$ is the surface current.

The MR wave analysis begins with a sequence of radar backscatter images that is obtained by interpolating from the polar measurement grid to the Cartesian analysis window coordinates. The radar image sequence is then transformed to the spectral domain using a 3D fast Fourier transform (FFT). In 3D wave number frequency space, (3) defines the so-called *dispersion shell* which resembles an inverted cone and gets distorted in the presence of a surface current (Young et al. 1985). If the waves and winds are favorable, i.e., a minimum significant wave height H_s of ~ 0.5 m and wind speed of ~ 3 m/s (Hatten et al. 1998), the 3D radar image spectrum $F_I(\mathbf{k}, \omega)$ resulting from the FFT shows a set of distinct peaks that are located on the dispersion shell. Figure 6a shows the dispersion shell for a 0.5 ms^{-1} current coming from 30° (clockwise from y-axis). The Nyquist frequency ω_{Ny} of 2.1 rads^{-1} defines the spectrum's upper frequency limit and is given by the antenna rotation rate.

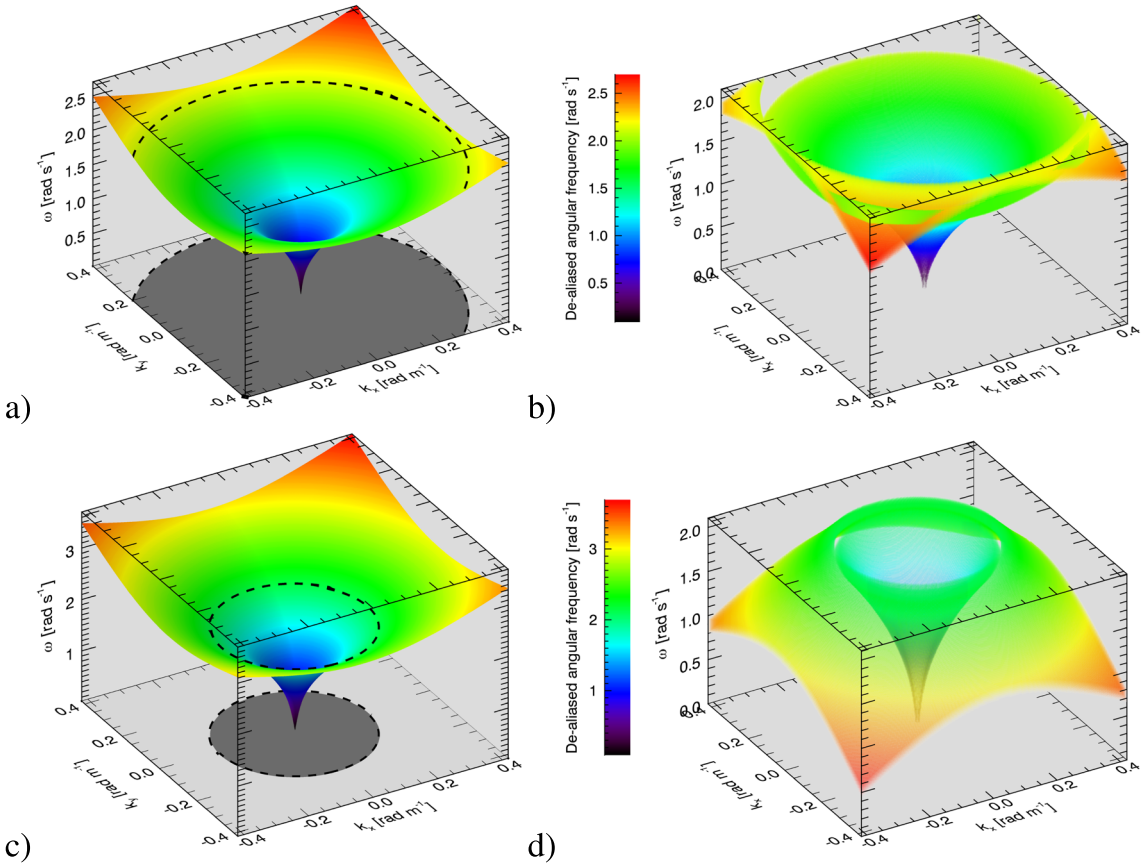

Fig. 6 Dispersion shells before and after unfolding of aliased wave energy for fundamental mode (**a**, **b**) and first harmonic (**c**, **d**). The *dashed curves* mark ω_{Ny} and encircle the wave numbers whose frequencies are within the Nyquist limit (*dark gray areas*) (**a**, **c**). The shells are shifted by a 0.5 ms^{-1} current coming from 30° (clockwise from *y*-axis)

From the image spectrum, first, the surface current is determined by means of a least-squares regression method that exploits the dispersion relationship (3) (Young et al. 1985). In addition to the sea–state energy located on the "fundamental mode" dispersion shell, the higher harmonic signal and the signal that is folded by temporal aliasing is considered for the least-squares method (Senet et al. 2001). The higher harmonics of the dispersion relation are believed to appear due to the nonlinearity of the MR imaging mechanism, especially shadowing effects, and are given by

$$S_p = \pm(p+1)\sqrt{\frac{gk}{p+1}\tanh\frac{kh}{p+1}} + \mathbf{k}\cdot\mathbf{U} \tag{4}$$

where the factor p is the order ($p = 0$ retrieves the fundamental) (Senet et al. 2001). Aliasing occurs if a signal is temporally (or spatially) undersampled, which is common for MR wave retrieval due to the relatively slow antenna rotation time (here, 1.5 s). To reconstruct the aliased signal, two symmetry conditions of the FFT are used: (1) the $2\omega_{Ny}$ periodicity given by

$$P(k_x, k_y, \omega) = P(k_x, k_y, \omega + n\omega_{Ny}) \tag{5}$$

and (2) the point symmetry to the point of origin (Seemann et al. 1997)

$$P(k_x, k_y, \omega) = P(-k_x, -k_y, -\omega) \tag{6}$$

Limited by ω_{Ny} (in contrast to Fig. 6a), Fig. 6b shows the aliased dispersion shell and its intersections with the fundamental mode shell, leading to ambiguities. Figure 6c and d illustrate the first harmonic's dispersion shell before and after consideration of the aliasing effect.

Figure 7 gives an example wave number–frequency slice taken from a 1-h averaged 3D radar image spectrum. The slice was extracted at $k_x = 0$ $radm^{-1}$, with surface waves and currents traveling along the *y*-axis (from right to left). The color scale is logarithmic to highlight the various contributions to the spectrum. As expected, the spectral coordinates that lie on the fundamental mode dispersion curve have the most power, but first and second harmonic contributions can also be easily distinguished. In addition,

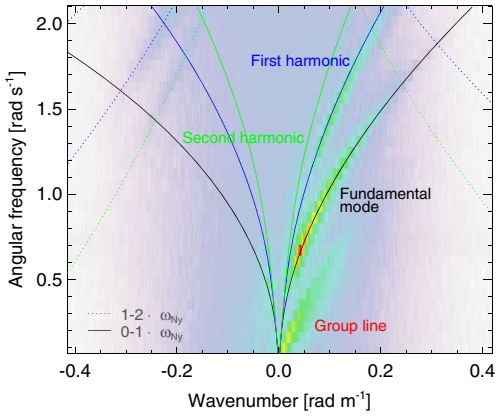

Fig. 7 Wave number–frequency slice taken from 1-h averaged 3D radar image spectrum. Data shown here were extracted at $k_x = 0$ radm^{-1}, with surface waves and currents traveling along the y-axis (from *right to left*). The *white-to-red color scale* is logarithmic. The *curves* corresponding to the dispersion relation's fundamental, first harmonic, and second harmonic modes are shown in *black*, *blue*, and *green*, respectively. The aliasing of above-ω_{Ny} wave energy is illustrated by the *dashed lines* (corresponding to frequencies from 1 to $2 \times \omega_{Ny}$)

the higher harmonics have aliased energy that is significantly above noise. Finally, the group line that is due to modulations by the group structure of the wave field contributes importantly to the overall spectral power (Frasier and McIntosh 1996). Here, to avoid group line contributions and remove the static pattern that is due to the backscatter intensity's range dependency (Borge and Soares 2000), frequencies below a threshold ω_{th} of ~ 0.5 rads^{-1} are disregarded.

Once the surface current is known, the dispersion relationship can be used to remove the spectral components that do not belong to the wave field from the image spectrum $F_I(\mathbf{k}, \omega)$, yielding the filtered 3D spectrum $F_F(\mathbf{k}, \omega)$ (Borge et al. 2008). To obtain an estimate of the 3D wave spectrum $F_W(\mathbf{k}, \omega)$, however, a further processing step is needed. This is because comparisons between MR image spectra and the corresponding spectra from in situ sensors have found differences due to the radar imaging mechanism's nonlinearities. Borge et al. (2004) propose the empirical wave number-dependent transfer function $T(\mathbf{k})$ to minimize the observed differences:

$$F_W(\mathbf{k}, \omega) = F_F(\mathbf{k}, \omega) \cdot T(\mathbf{k}) \tag{7}$$

Integrating the resulting 3D wave spectrum $F_W(\mathbf{k}, \omega)$ over the frequency yields the 2D wave number spectrum (Borge et al. 2008)

$$F_W(\mathbf{k}) = \int_{\omega_{th}}^{\omega_{Ny}} F_W(\mathbf{k}, \omega) \mathrm{d}\omega \tag{8}$$

A final challenge is that H_s cannot be directly retrieved from MR image spectra. For $F_W(\mathbf{k})$ to give the correct surface height spectral density, it needs to be calibrated. Studying satellite synthetic aperture radar (SAR) data, (Alpers and Hasselmann 1982) were the first to propose a proportionality between H_s and the radar backscatter's signal-to-noise ratio SNR. Similarly, (Ziemer and Dittmer 1994) found for MR data that

$$H_s = a + b\sqrt{SNR} \tag{9}$$

where a and b are proportionality constants. In contrast to SAR, the MR SNR is derived from the 3D radar image spectrum. Borge et al. (2008) provide the following exact definition:

$$SNR = \frac{\int_{\Omega_{\mathbf{k}}^{\alpha}} F_W(\mathbf{k}) \mathrm{d}^2 k}{\int_{\Omega_{BGN}} F_{BGN}(\mathbf{k}, \omega) \mathrm{d}^2 k \mathrm{d}\omega} \tag{10}$$

Here, the 3D background noise spectrum is given by

$$F_{BGN}(\mathbf{k}, \omega) = F_I(\mathbf{k}, \omega) - F_F(\mathbf{k}, \omega) - F_{HH}(\mathbf{k}, \omega) \tag{11}$$

where $F_{HH}(\mathbf{k}, \omega)$ is obtained by filtering all but the higher harmonic spectral components within $F_I(\mathbf{k}, \omega)$. The wave signal integration domain $\Omega_{\mathbf{k}}^{\alpha}$ in Eq. (10) applies the power threshold $\alpha \cdot \max[F_W(\mathbf{k})]$ to limit background noise contributions from the dispersion shell. The background noise integration domain Ω_{BGN} is limited by ω_{th} to avoid the static pattern and group line contributions.

All the wave parameters that we study in the following sections are derived from the 2D frequency-direction spectrum which is related to $F_W(\mathbf{k})$ by

$$E(f, \theta) = F_W(\mathbf{k}) k \frac{\mathrm{d}k}{\mathrm{d}\omega} \tag{12}$$

The frequency f is given by $\omega/(2\pi)$ which is a function of $\mathbf{k}$ (3) and θ is the angle of $\mathbf{k}$. The factor $k\mathrm{d}k/\mathrm{d}\omega$ is the Jacobian between the two-coordinate systems (k_x, k_y) and (f, θ) (Young et al. 1985). The 1D frequency spectrum is given by

$$E(f) = \int_0^{2\pi} E(f, \theta) \mathrm{d}\theta \tag{13}$$

the directional moments by

$$A_n(f) + i B_n(f) = \frac{1}{\pi} \int_0^{2\pi} \exp(in\theta) E(f, \theta) \mathrm{d}\theta \tag{14}$$

the mean direction by

$$\theta_m(f) = \tan^{-1} \frac{B_1(f)}{A_1(f)} \tag{15}$$

the spreading direction by

$$\sigma(f) = \sqrt{2(1 - \sqrt{A_1(f)^2 + B_1(f)^2})} \tag{16}$$

the peak wave period by

$$T_p = \frac{1}{f_p} \quad \text{where} \quad f_p = \max_f[E(f)] \tag{17}$$

and the peak wave direction by

$$\theta_p = \theta_m(f_p) \tag{18}$$

The Datawell buoy's significant wave height, which is used to calibrate the MR record, is given by

$$H_s = 4\sqrt{m_0} \tag{19}$$

where the variance $m_0 = \int_0^\infty S(f)\mathrm{d}f$ (O'Reilly et al. 1996; COST Action 714 2005).

4 Analysis and results

This section analyzes the dependency of the MR surface wave retrieval on range and azimuth. The importance of the azimuth dependency becomes evident just by inspecting the strength of the wave signal within the different analysis windows shown in Fig. 5: while the long wave signal in the window towards the bow is well pronounced, it is considerably weaker in both starboard and port-side. However, while (Reichert 1994) has investigated the azimuth dependency of the MR sea surface backscatter, to this date, no quantitative analysis of the MR wave results' dependency on both range and azimuth has been published. We believe that this dependency negatively affects results, in particular for shipboard MRs. The goal of this study is therefore to improve our understanding of the MR wave results' range-azimuth dependency and to develop techniques that correct for it.

Here, we analyze data that were collected during a 12-h period starting June 14, 2010 at 00:00 UTC. During this period, the wind (measured just under the radar antenna at a height of $\sim$ 30 m) was blowing from north–northwest, starting at $\sim$ 10 ms^{-1} to peak at $\sim$ 18 ms^{-1} around $t = 6$ h after which it decreased to 15–16 ms^{-1}.

In Section 4.1, we explain the design of our range-azimuth dependency study. Section 4.2 investigates how varying the analysis window range and azimuth affects the 3D radar image spectra. The influence on surface wave parameters is studied in Section 4.3. MR wave spectra and their range-azimuth dependency is analyzed in Section 4.4. Section 4.3 and 4.4 also compare the MR wave results with the Datawell buoy measurements and propose new techniques to correct for the range-azimuth dependency.

4.1 Study design

The MR data recorded from FLIP during Hi-Res is particularly well suited for our study of the wave results' range-azimuth dependency. This is because the radar was installed with an unobstructed 360°-wide FOV, which from our experience is quite unusual. The full radar FOV allows us to consider all possible angles between analysis window and peak wave direction. (An unobstructed view of the sea surface also allows for highly accurate radar-based wind estimates, as shown by Lund et al. (2012a) using the same data set.)

To study the MR wave results' dependency on range and azimuth, we devised three rings of analysis in the near-, mid-, and far-range (centered around ranges of 750, 1,470, and 2,910 m, respectively). Each ring consists of 12 square analysis windows that are evenly distributed over all azimuths. The analysis window edge lengths of 480, 960, and 1,920 m for near-, mid-, and far-range, respectively, were chosen such that there is zero range- and only limited azimuth overlap between neighboring windows. Figure 8 illustrates the study setup. The radar image shown in the figure was collected from FLIP during our 12-h analysis period, at $t = 5$ h. As is clear from the figure, our study is designed such that the whole radar FOV is covered by analysis windows.

It may be argued that the increasing analysis window edge length from near- to far-range introduces a bias. We believe, however, that such setup is justified for the following two reasons: Firstly, each analysis window, independent of range, covers the same azimuthal width of $\sim$ 30°. Secondly, the radar backscatter characteristics change much more rapidly in the near- than they do in the far-range. This can be explained by the radar equation, according to which the decay of the backscattered power with range is cubic (Gommenginger et al. 2000). What is more, despite an analysis window edge length that increases with range, the range of incidence angles covered by the near-range analysis ring (from 86.6 to 88.3°) is wider than it is in mid- (88.3 to

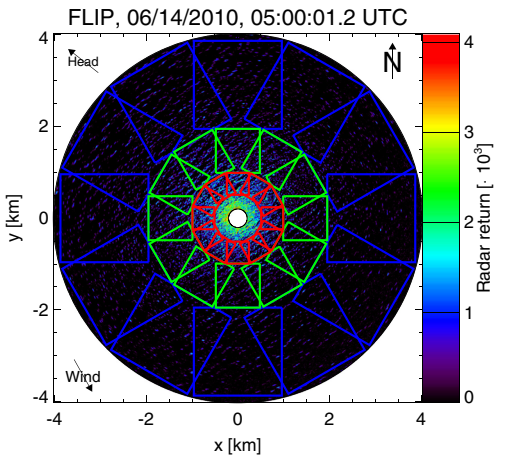

Fig. 8 Analysis window setup for study. At each range increment, 12 slightly overlapping windows are set to sample wave conditions, covering all antenna look directions. The near-range analysis windows are plotted in *red*, the mid-range in *green*, and the far-range in *blue*

89.1°) and far range (89.1 to 89.6°). Our study design therefore ensures that the sea clutter within each analysis window is reasonably homogeneous.

Finally, note that in the following sections, we assume the surface wave field to be homogeneous within the entire radar FOV. This is important because otherwise, we would not be able to unambiguously attribute the observed differences in the MR wave results to changes in range and azimuth. Since FLIP was moored at a site with an only mildly sloping bathymetry and the radar's maximum range is relatively small ($\sim$ 4 km), we believe that assuming spatial homogeneity is reasonable.

4.2 3D radar image spectra

As we explained in Section 3, the MR surface wave analysis begins by transforming a sequence of backscatter images to the spectral domain. Here, as in the following sections, we use sequences of 64 radar images, i.e., $\sim$ 1.5 min of data. For each analysis window, after discarding the negative frequencies that contain no additional information, we retain 33 directionally unambiguous 2D wave number spectra at angular frequencies ranging from zero to the Nyquist frequency ω_{Ny} (2.1 rads^{-1}). This section provides a qualitative analysis of how the 3D radar image spectra differ as a function of range and azimuth. In particular, we will be looking at the spectral shapes of the wave signal, the nonlinear contributions, and the background noise.

It has already been pointed out by Senet et al. (2001) that the MR surface current (and wave) results could be improved significantly if the shape of the background noise were known. This is because for high wave numbers, the spectral density is significantly reduced, which is why a constant power threshold is not the proper quantity to separate signal from noise. For future work, they therefore propose to develop a 2D fitting algorithm to parameterize the shape of the spectral background noise. To our knowledge, little work has been done towards this goal since then. One notable exception is a study by Borge et al. (2008), who analyzed the structure of the different contributions to the MR image spectrum, with a special focus on the background noise, in order to derive the significant wave height H_s. To determine the background noise's dependency on the wave number, they integrated the 3D background noise spectrum (11) first along the ω-axis and then over all the wave number directions $\theta = \tan^{-1}\left(\frac{k_y}{k_x}\right)$

$$F_{BGN}(k) = \int_0^{2\pi} \int_{\omega_{th}}^{\omega_{Ny}} F_{BGN}(\mathbf{k}, \omega) \mathrm{d}\omega k \mathrm{d}\theta \tag{20}$$

where ω_{th} is used to avoid the static pattern and group line contributions and the factor k inside the integral is the Jacobian needed to change from Cartesian (k_x, k_y) to polar coordinates (k, θ). Similarly, they determined the noise's dependency on the frequency by

$$F_{BGN}(\omega) = \int_{\Omega_{\mathbf{k}}} F_{BGN}(\mathbf{k}, \omega) \mathrm{d}^2 k \tag{21}$$

Borge et al. (2008) found that the background noise spectrum presents significantly higher values for lower wave numbers, decaying as the wave numbers are increasing. For high wave numbers ($k > 0.23$ radm^{-1}), the spectral density reaches a constant value, which they identify as the sensor system's thermal noise. Regarding the background noise's frequency spectrum, they showed that for $\omega > \omega_{th}$, the spectral energy values are almost constant. This is seen to be consistent with the fact that speckle noise is temporally uncorrelated. However, they do not investigate the dependency of the spectral density on the wave number direction θ or, for that matter, the background noise's dependency on analysis window range and azimuth.

Figure 9 shows a selection of frequency slices (0.05 s^{-1}, 0.10 s^{-1}, and 0.31 s^{-1}) that were taken from 1-h averaged 3D radar image spectra. We chose to average our 3D spectra in order to reduce the effect of speckle noise, allowing us to better focus on the spectrum's main contributions. The figure's three columns correspond to the near-, mid-, and far-range analysis windows (roughly) in upwave direction, respectively. The data shown in the figure were collected starting from $t = 5$ h. During this period, the significant wave height H_s was above 3 m and the wind was blowing at a speed of 17 ms^{-1} coming from the north–northwest. The radar-derived surface current was 0.51 ms^{-1} in a southern direction, agreeing well with our expectations for a wind-driven surface current, in that the speed is $\sim$ 3 % and the direction is shifted clockwise relative to the mean wind for that period.

Note that the spectra are plotted in analysis window coordinates where the k_y-axis corresponds to the line that connects the image origin to the analysis window's center point. This means that, since the windows were oriented roughly upwave (and upwind; i.e., 330°) clockwise from north), the current direction in the figure is 210° and the wind is coming from 0° (clockwise from the k_y-axis). The spectra were logarithmically transformed and then individually scaled to improve the visibility of weak features.

For a given frequency, in absence of a current, the dispersion relationship (3) is represented by a circle with radius $|\mathbf{k}|$ and origin $k_x = k_y = 0$ radm^{-1}. If a current is present, the circle gets distorted and the dispersion curve takes on an elongated shape. The mid-range 3D radar image spectrum has its peak spectral density within the 0.10 s^{-1} frequency slice. The near- and far-range spectra have their respective energy peaks at nearby locations. This signal is due to the peak wave system, it is located on a narrow band of wave numbers in vicinity of the fundamental mode dispersion

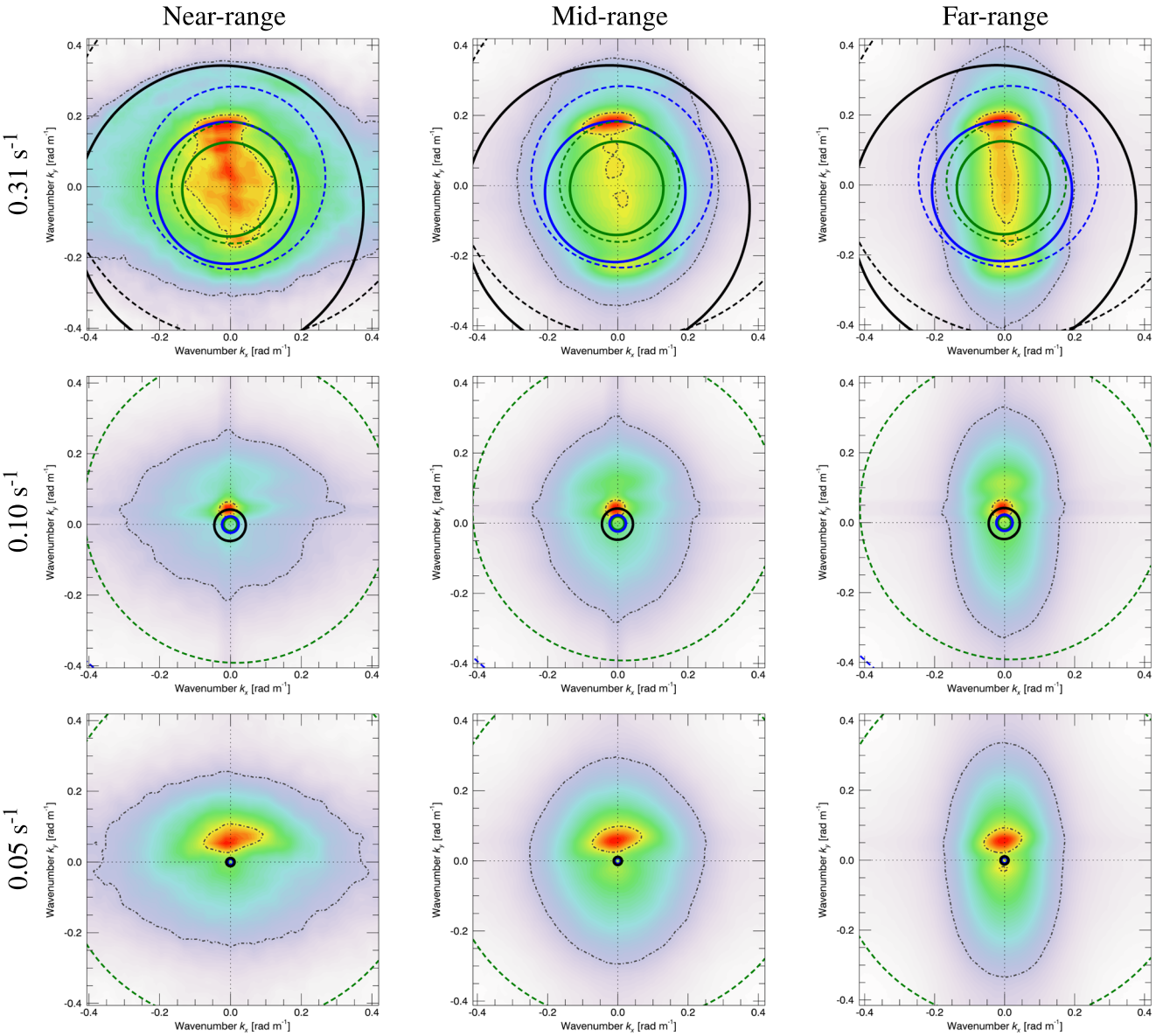

Fig. 9 Selection of frequency slices extracted from 1-h averaged 3D radar image spectra of near-, mid-, and far-range analysis windows in upwave direction. The *bottom*, *center*, and *top rows* correspond to frequencies of 0.05, 0.10, and 0.31 s^{-1}, respectively. The *left*, *center*, and *right* columns correspond to the near-, mid-, and far-range analysis windows, respectively. The *white-to-red color scale* is logarithmic. The *curves* corresponding to the dispersion relation's fundamental, first harmonic, and second harmonic modes are shown in *black*, *blue*, and *green*, respectively. The aliasing of above-Nyquist-frequency wave energy is illustrated by the *dashed lines* (corresponding to frequencies from 1 to 2×ω_{Ny})

curve (shown in black), and it clearly dominates all other spectral contributions independent of range.

The dispersion relationship's higher harmonics (4) experience a current-induced Doppler frequency shift just as the fundamental mode does. Figure 9 shows the dispersion curves for the first harmonic in blue and the second harmonic in green. The higher harmonic contributions are clearly visible within the 0.31 s^{-1} frequency slice. At that frequency, the first harmonic dominates the signal over all ranges. Coming from the same direction as the peak wave system (clearly visible on the fundamental mode dispersion curve at 0.10 s^{-1}), it also spreads over a similarly narrow range of directions. A much less energetic and narrower peak, but still in peak wave direction, can be observed on the second harmonic's curve, most distinctive in the far range. Also at the far- and (to a somewhat lesser extent) mid-range analysis window, the aliased wave signal associated with the first and second harmonic dispersion curves (blue and

green dashed, respectively) is most visible (roughly at (0.00, −0.15) and (0.00, −0.25) rad m^{-1}. If the aliased higher harmonic wave signal is reconstructed to its original frequency, it propagates roughly in the same direction as the peak wave system. The fact that it appears to come from the opposite direction can be explained by the symmetry conditions given in Eqs. 5 and 6 Seemann et al. (1997).

The relative importance of the higher harmonic signal for the different ranges becomes most evident by comparing it to the fundamental mode peaks. With this goal in mind, let us revisit the high-frequency slices. In the near range, the fundamental mode dispersion ring shows a faint but distinct above-noise wave signal (e.g., at (0.15, 0.35) rad m^{-1}). But in the mid range, the wave signal becomes difficult to distinguish from the noise, and it is completely absent in the far range. While our ability to image the short waves decreases with range, the higher harmonics gain prominence. As mentioned in Section 3, the higher harmonics are attributed to nonlinearities in the imaging mechanism, in particular shadowing (Senet et al. 2001). As the radar incidence angle increases with range, so does the importance of shadowing, which is why the observed range dependency of the higher harmonic signal could be expected. Also, shadowing tends to enhance the long-wave signatures, while it weakens those of the short waves. It is therefore no surprise that the (high wave number) fundamental mode signal is best visible in the near range.

Finally, the 0.05 s^{-1} frequency slices in Fig. 9 illustrate the group line contributions for the different analysis window ranges. In all three cases, the group line contribution is highlighted by the inner contour line (*dash-dotted gray*). What resembled a line in Fig. 7 would be more accurately described as a *group cloud* when studied in all three dimensions. However, to achieve consistency with previous works (e.g., Frasier et al. 1996), we will keep using the term *group line*. The low-frequency spectra give rise to the following additional observations: (1) The far-range group line covers a much narrower band of directions than the near range one. (2) By comparing the location of the secondary peak in the far-range 0.10 s^{-1} frequency slice to that of the group line dominating the 0.05 s^{-1} frequency slice, we conclude that this secondary peak represents an extension of the group line. This, combined with the fact that the secondary peaks at 0.10 s^{-1} are much less pronounced in the mid range and hardly discernible in the near-range spectrum, in turn suggests that the group line is more prevalent in the far than it is in the near range. From this it follows that the group line is not only due to intermodulations between different wave field components but also enhanced by the imaging mechanism's nonlinearities, in particular shadowing.

One last note on Fig. 9 is in regards to the shape of the background noise, which is highlighted by the outer contour line (*dash-dotted gray*) in all spectra. We can confirm the finding by Borge et al. (2008) that the background noise decreases from small to high wave numbers and is fairly constant as a function of frequency when considered outside of the group line's and static pattern's range of influence (the former observation can be made from the figure, the latter is not shown here). However, the elliptical shape of the outer contour lines indicates that the background noise not only depends on $|\mathbf{k}|$ but also on the wave number direction θ. Also, the shape's orientation clearly depends on range. Using the terminology for an ellipse, the major axis is oriented along the k_y-axis in the mid and far range, but in the near range, it follows the k_x-axis. To our knowledge, neither the background noise's dependency on the wave number direction θ nor its range-azimuth dependency have previously been discussed in the literature.

To further investigate the background noise's dependency on θ, Fig. 10 shows the far-range wave number spectra at a frequency of 0.31 s^{-1} for a crosswave (240° clockwise from north) and the downwave analysis window orientation (150°). Note that both spectra are plotted in analysis window coordinates, which explains why in the downwave case the dominant first harmonic contribution now appears to travel in the opposite direction compared to the upwave situation studied in Fig. 9. What is most remarkable in this figure, however, is that for both cross- and downwave examples the orientation of the background noise ellipsoid is still along the k_y-axis. Clearly, the background noise's shape, at least in the far range, depends mostly on the analysis window orientation, apparently unaffected by the relative wave (and wind) direction. Figure 10 also demonstrates to what extent the wave signal is weakened in the crosswave direction. While the downwave spectrum (not too different from its upwave counterpart) shows a clear first harmonic and a weak second harmonic contribution as well as some evidence of aliasing, the crosswave spectrum shows no wave signal whatsoever.

To summarize, the peak wave system is responsible for the strongest 3D spectral contribution, independent of range and azimuth. The MR image spectrum's range dependency is most evident when considering the upwave spectra's low and high frequency ends. At the low end, we observed that the group line gains importance with range. At the high frequency end, a short-wave signal is clearly visible only in the near range and absent in the far range. In contrast, the higher harmonic wave signal, attributed to the imaging mechanism's nonlinearities, is best defined in the far range. We also demonstrated that the background noise depends on the wave number vector (magnitude and direction) as well as on analysis window range and orientation. Finally, we showed that the wave signal is strongly influenced by the analysis window orientation. This becomes evident when comparing the far-range high-frequency crosswave spectrum with its downwave counterpart: while the

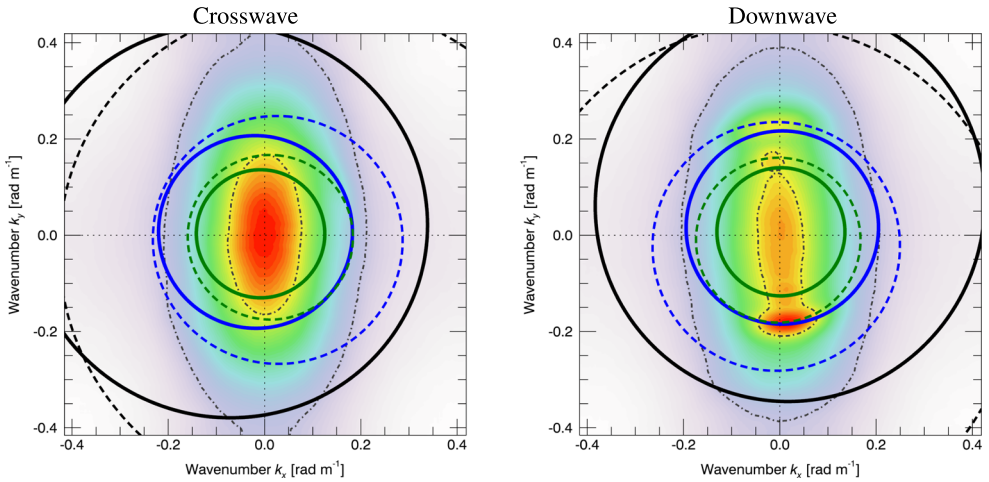

Fig. 10 Frequency slices extracted from 1-h averaged 3D radar image spectra of far-range analysis windows in cross- and downwave directions. Both plots correspond to a frequency of 0.31 s^{-1}. The *white-to-red color scale* is logarithmic. The *curves* corresponding to the dispersion relation's fundamental, first harmonic, and second harmonic modes are shown in *black*, *blue*, and *green*, respectively. The aliasing of above-Nyquist-frequency wave energy is illustrated by the *dashed lines* (corresponding to frequencies from 1 to 2 × ω_{Ny})

noise effectively obscured all surface wave signal in the crosswave case, higher harmonic contributions are clearly visible when looking downwave (or, for that matter, upwave).

4.3 Surface wave parameters

As the previous section demonstrated, the strength of the surface wave signal in the 3D radar image spectra strongly depends on range and azimuth. The FFT-based method for determining the wave (and current) information within MR image sequences was described detailedly in Section 3. In this section, we investigate whether the observed spectral dependency on range and azimuth takes a toll on the MR-retrieved peak wave parameters.

As mentioned above, the dependency of MR surface wave estimates on antenna heading was first investigated by Reichert (1994). However, to our knowledge, the range dependency remains unexplored in the literature. Furthermore, no correction scheme to address either dependency has yet been proposed. Our goal here is therefore, not only to describe the MR surface wave results' range-azimuth dependency, but also to develop new methods to remove it where possible.

We begin by examining the 1-h averaged bulk wave parameters determined for the same period studied in the previous section, starting at $t = 5$ h. Figure 11 shows the signal-to-noise ratio SNR, the peak wave period T_p, and peak wave direction θ_p as functions of range and azimuth. The figure prompts a number of observations for each parameter.

SNR, which is used to determine the significant wave height H_s (10), has a dominant peak upwave, a second smaller peak downwave, and troughs in the two crosswave directions. The difference between the up- and downwave peak can be explained by the imaging mechanism: the surface roughness elements that are responsible for the backscatter (Bragg waves and micro-breakers) are concentrated on the forward face of the wave, and thus more (less) prominent as the radar looks upwave (downwave) (Plant 1989). The crosswave troughs can be explained by the fact

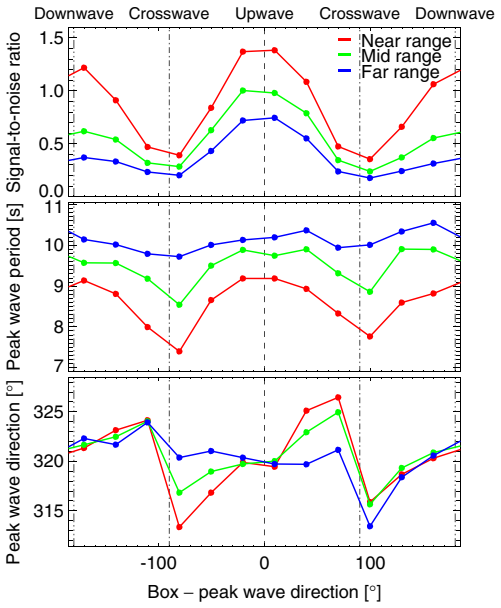

Fig. 11 Signal-to-noise ratio, peak wave period, and peak wave direction as functions of range and azimuth (for 1-h period, centered around $t = 5.5$ h). The *vertical lines* mark the upwave, crosswave, and downwave directions. The near-, mid-, and far-range results are shown in *red*, *green*, and *blue*, respectively

that the MR scatterers are mostly oriented in wind direction (Lund et al. 2012b). While the above characteristics apply to all ranges, SNR decreases from near to far range with inter-range differences being most marked up- and downwave.

T_p's dependency on the analysis window orientation shows some similarity with that of SNR, in that it has two peaks up- and downwave and troughs crosswave (less markedly so in the far range). There is also a significant dependency on range, with the near-range T_ps up to ~ 2 s shorter than the far-range ones. The range dependency has a straight-forward explanation: shadowing by the wave crests is much more pronounced in the far than in the near range. The stronger the shadowing effect, the more the short waves are suppressed and the long waves enhanced. As a result, T_p appears to increase from near- to far-range. The dependency on azimuth is more complicated, but may be due to the fact that each analysis window is best at imaging the waves that are traveling towards it. This concept is easiest to understand if one imagines a radar first looking upwave (perpendicular to the wave crests) and then crosswave (parallel). The radar's wave imaging mechanisms (Bragg scattering, tilt modulation, and shadowing) are most effective in the former and greatly compromised in the latter case. As a result, the spectral peak is more pronounced up- and downwave than it is crosswave. What we still cannot explain is why the peak is at lower and higher frequencies, respectively. Nonetheless, we think that the observed azimuth dependency must, to first order, be interpreted as an artifact induced by the radar imaging mechanism. However, to a limited extent, it may also be reflective of the wave field components that are traveling in (or against) the given analysis window direction.

Finally, θ_p has a clear (if small, note the axis range) dependency on azimuth. As with T_p, the observed patterns probably result from the fact that each analysis window "favors" the waves that are traveling towards it. In our case, the azimuthally-averaged θ_p is $\sim 320°$ (clockwise from north). The analysis window pointing west will therefore be biased westward (i.e., smaller directions, relative to mean θ_p), while the one pointing north will be biased towards waves coming from north (i.e., directions greater than the mean θ_p). As the analysis windows pass from crosswave towards downwave, their biases regarding the peak wave system reverse suddenly. For example, the window pointing east will now "favor" waves coming from west (i.e., directions smaller than the mean θ_p). Interestingly, the observed azimuth dependency for θ_p perfectly reproduces the bias we would expect from this mechanism. However, since the θ_ps correspond to different T_ps, a clear causal relationship cannot be established. As far as θ_p's dependency on range is concerned, it is noteworthy that the previously described behavior is most (least) evident in the near (far) range.

Figure 12 shows the 1-h averaged mid-range surface wave parameters as functions of azimuth and time, covering the first 6 h of our study period. During this period, the wind speed increased from ~ 10 to 18 ms^{-1} and the significant wave height H_s from 2.1 to 3.2 m. The figure illustrates that the dependencies identified above for $t = 5.5$ h (Fig. 11) persist through time, even as H_s increases. For SNR, it can be observed that the difference between the up- and downwave values becomes more marked with time (and growing H_s). The SNRs determined for the crosswave directions are much less sensitive to changes in H_s. Note also that SNR can be up to four (two) times larger for an analysis window that is positioned upwave as opposed to crosswave (downwave). While T_p is seen to increase with time, its azimuth dependency remains essentially unchanged. The same applies to θ_p, which exhibits fairly constant dependencies over time. Importantly, both the T_p and θ_p dependencies are symmetric over 180°, which is a property that we will exploit for our correction scheme.

Now, what do these findings imply for operational MR wave retrieval? Ideally, for a given range, the wave analysis windows should be distributed evenly over all directions. Then, to remove the azimuth dependency, the results from the different windows could simply be averaged. But the radar FOV is typically partially obstructed, limiting the area that can be used for wave retrieval. In such case, the wave analysis windows cannot cover all directions and, if the azimuth dependency is ignored, averaging the results from all available windows is likely to produce an increased variability or error.

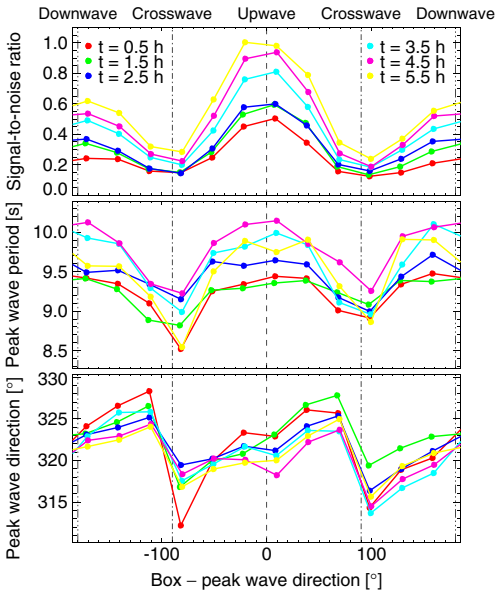

Fig. 12 Signal-to-noise ratio, peak wave period, and peak wave direction for mid-range as functions of azimuth. Each *curve* corresponds to a 1-h average, time is color-coded

To better explain this assertion, let us revisit our example of a MR station aboard a research vessel where a 50°-wide section of the radar FOV towards the stern is blocked by superstructures and three analysis windows are placed towards the bow, to the port, and to the starboard side of the hull. The latter two are slanted aftward, such that the available 310° are covered fully if all windows are combined (see Section 3, Fig. 5). With this setup, if the ship changes course from up- to downwave – which may happen frequently on research vessels –, the mean SNR across the three analysis windows will decrease. This translates into an artificial H_s decrease, unless some correction scheme is implemented. In contrast, for this particular course change, the peak wave period T_p and peak wave period θ_p would remain unchanged. However, if the ship instead changes heading by, e.g., 45° counter-clockwise, both T_p and θ_p will increase. If the heading changes by the same amount but clockwise, T_p will still increase, but θ_p will decrease. Note that the azimuth dependency is less of an issue at coastal stations where waves generally travel towards the shore, and more difficult to notice on fixed offshore platforms where the resulting error is of a more gradual nature. This may be why, to our knowledge, none of the available commercial wave radars correct for this phenomenon.

To remove the azimuth dependency from the MR significant wave height H_s estimates, we propose to no longer average over the results from all windows but instead use either the upwave or downwave signal-to-noise ratio SNR. Figure 13 shows the same 6-h worth of SNR data presented in Fig. 12, but now, together with the best-fit curves, we obtained by least-squares fitting a Fourier series to each dependency. The advantage of such least-squares regression method is that it enables us to determine the upwave and/or downwave peak SNR values that we can then use to retrieve H_s. In addition, by including all available SNR values, it allows us to reduce the detrimental effects of outliers.

As discussed in Section 3, to retrieve H_s from MR image spectra, we need to determine the best-fit line that links $\sqrt{SNR}$ to a reference H_s measurement (10). Figure 14 shows a scatter plot of the Datawell H_s measurements and mid-range SNR values at the up- and downwave location.

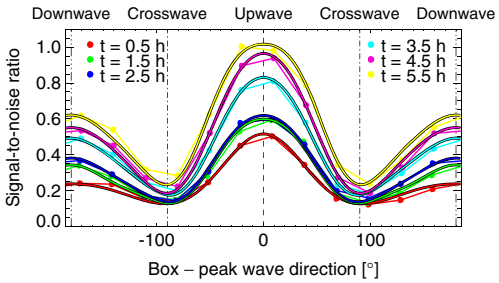

Fig. 13 Measured and fitted mid-range signal-to-noise ratio curves as functions of azimuth. Each *curve* corresponds to a 1-h average

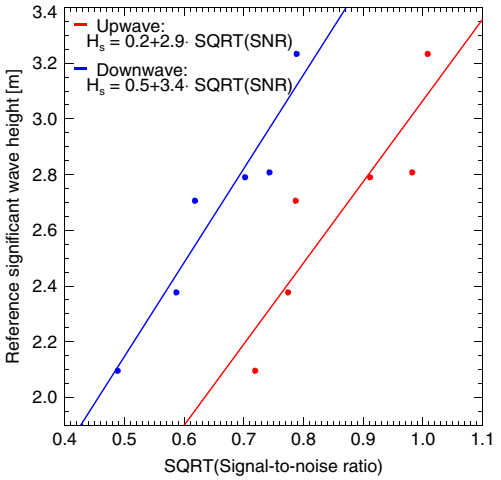

Fig. 14 Best-fit calibration lines to determine the significant wave height from the square-roots of the mid-range least-squares fitted signal-to-noise ratios at the up- and downwave location. The significant wave height measurements were obtained from the nearby Datawell buoy. Considered are the first 6 h of the study period

The SNR values were retrieved from the least-squares fitted Fourier series shown in Fig. 13. The figure also shows the best-fit lines and gives the calibration constants for both the up- and downwave case.

To remove the azimuth dependency from our T_p and θ_p estimates, we propose an even simpler approach. As shown above (Figs. 11 and 12), both parameters' dependencies exhibit a 180°-symmetry. The azimuth dependency can therefore be removed by averaging over the wave results from analysis windows that cover either 180 or 360° of the radar FOV. Surface wave parameters that were determined by averaging over the results from analysis windows that cover an area other than 180 or 360° will depend on the windows' relative angle to the waves. Figure 15 illustrates the

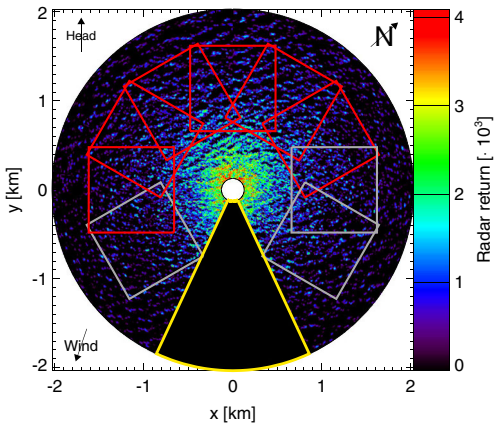

Fig. 15 Example of a single radar image with blacked-out section (*yellow frame*) where the radar FOV is obstructed. Analysis windows cover the entire radar FOV, but surface wave results should be derived from the analysis windows marked in *red* only

recommended analysis window setup for our example case with a 50°-wide aftward shadow. The surface wave retrieval should be limited to the six analysis windows that are shown in red and cover 180°. While some freedom remains as to which windows to choose, it is advisable, if possible, to center the windows around the upwind direction because that is where the radar backscatter from the sea surface is strongest (Lund et al. 2012b).

Here, since we have the fortune of a completely unobstructed view of the sea surface, we average over the wave results from all 12 analysis windows, covering 360° (see Fig. 8). Such full coverage is preferable, as it allows us to double the area that is analyzed, helping to reduce the variability of the surface wave estimates. Figure 16 shows a time series of the MR azimuthally-averaged wave parameters H_s, T_p, and θ_p from near to far range and the corresponding Datawell buoy measurements covering our full 12-h study period. The figure also shows concurrent wind data that were acquired from FLIP and corrected to 10 m above sea surface.[1] The near and far range H_s calibration constants were determined from the first 6 h of data in the same fashion as described above for the mid range. In all three cases, the least-squares fitted upwave (as opposed to downwave) SNR values were used. The agreement between MR and Datawell wave measurements is, overall, very good. The seemingly high variability of the MR estimates is due to the fact that each data point was obtained from $\sim$ 1.5 min of radar backscatter measurements only. Regarding T_p, the mid range MR estimate agrees notably better with the reference data than the near and far range estimates do. MR and Datawell measurements of θ_p are roughly in wind direction, with a slight bias that is more pronounced for the buoy measurement. However, compared with wave sensor evaluations from the literature, the observed differences between the MR and buoy measurements fall within the expected range of $\sim$ 10° (Wyatt et al. 2003; Collins et al. 2013).

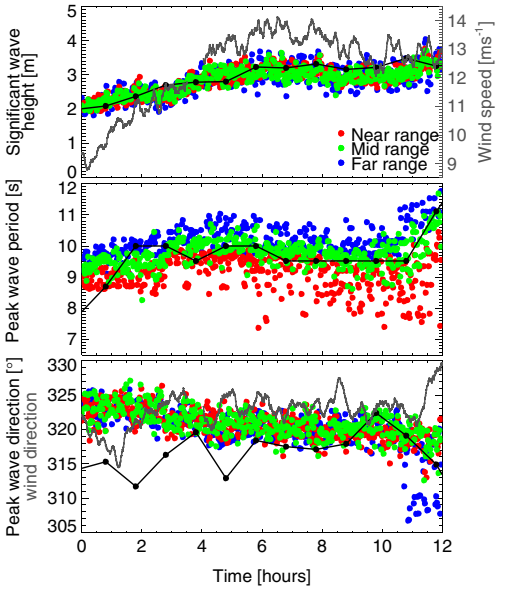

Fig. 16 Time series of peak wave parameters measured by MR at all three ranges and Datawell buoy. Corresponding FLIP-based anemometer measurements, corrected to 10 m above sea surface, are shown in *gray*

4.4 Surface wave spectra

In the previous section we discussed the surface wave parameters' azimuth-range dependency. Here, we investigate the wave spectrum's dependency on range and azimuth. This section also compares the MR wave spectra with the Datawell buoy reference data. An important advantage of MRs over traditional heave–pitch–roll buoys is that they can measure fully-directional wave spectra, meaning they are able to detect multi-modal seas. Buoys do not measure the 2D wave spectrum, but only a "1.5-D" spectrum that can, at best, resolve bimodal seas (e.g., Kuik et al. 1988; OReilly et al. 1996).

Figure 17 illustrates the azimuth dependency of our 1-h averaged mid-range frequency-direction spectra for $t = 5.5$ h. In particular, the figure shows spectra for the analysis windows that were oriented upwind, cross-wind, upswell, and cross-swell. Each spectrum was scaled to have the same energy content (significant wave height). A logarithmic scale was chosen to visualize the full range of variability. As could be expected from the previous section's findings, the wind sea (coming form north–northwest) is the dominant system in all directions. However, it is significantly weaker in cross-wind direction, where, as a result, the swell system (from south) becomes relatively more important. What is more, the cross-wind spectrum's wind sea system appears broadened due to its weakened peak. The cross-swell spectrum prompts another observation that is of interest, which is that the swell is completely absent. A similar finding was made by Hessner and Hanson (2010), who analyzed MR data collected at Duck, NC. They showed that the wind sea, which was in their case much less energetic than the swell, could only be observed in a narrow upwind area within the radar FOV. These results once again stress the importance of the wave retrieval's azimuthal dependency. Finally, the wave-like patterns within the high-frequency end of the spectra are a point of concern. The astute reader will have noticed that each spectrum shows two high-frequency peaks that are located in and against the direction the respective analysis window was oriented in. This finding agrees with our observations regarding the background noise within the 3D radar image spectra and its azimuthal dependency (Section 4.2, Fig. 10),

[1]The anemometer data were kindly provided by Luc Lenain, Scripps Institution of Oceanography.

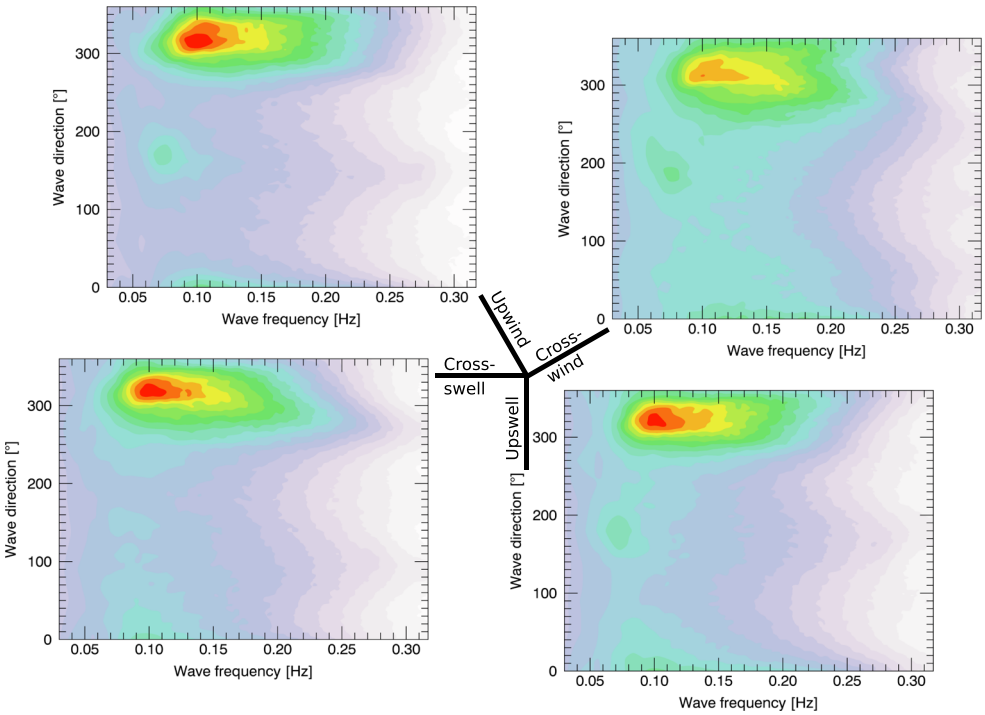

Fig. 17 Mid-range frequency-direction spectra on a logarithmic *white-to-red color scale* for upwind, cross-wind, upswell, and cross-swell azimuths (averaged over 1-h period, $t = 5.5$ h)

which should not be a surprise since the wave spectra are derived from them (Section 3, 7 to 12). We see the following problem here: it is not clear that the spectra's high-frequency region truly represents the surface wave field. In fact, the patterns' strong azimuthal dependency suggests that they are much more likely due to noise. Further research on the background noise characteristics is necessary before a definite conclusion can be drawn.

The 2D wave spectrum's dependency on range is analyzed in Fig. 18. The figure shows the 1-h averaged near- and far-range frequency-direction spectrum obtained with the analysis window oriented upwind for $t = 5.5$ h. The corresponding mid-range spectrum is shown in Fig. 17. From near- to far-range, it can be seen that the peak of the dominant wind sea system shifts from right to left, which is in agreement with our finding from Section 4.3 that the peak period increases with range. The growing importance of the swell and weakening of the wind sea with range further suggest that the far (near) range puts greater weight on long (short) waves. Finally, the wave-like pattern in the spectra's high-frequency region, that we hypothesized above to be mostly due to background noise, is much more pronounced in mid to far range than in near range.

In the following, our MR wave spectra are averaged over all azimuths. This effectively removes the wave results' azimuth dependency, allowing us to focus solely on the range dependency. Figure 19 shows the radar's azimuthally-averaged mid-range frequency-direction spectrum corresponding to the 1-h period that is centered around $t = 5.5$ h. A logarithmic scale was chosen to better represent the full range of spectral power. The spectral peak is located at $\sim$ (0.1 s^{-1}, 320°). A swell system with a frequency of $\sim$ 0.07 s^{-1} is coming from the south. Interestingly, as

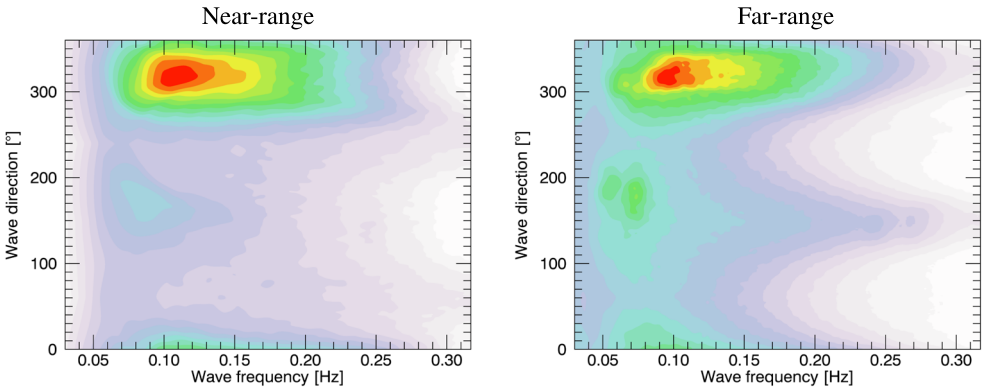

Fig. 18 Upwind frequency-direction spectra on a logarithmic *white-to-red color scale* for near- and far-range (averaged over 1-h period, $t = 5.5$ h)

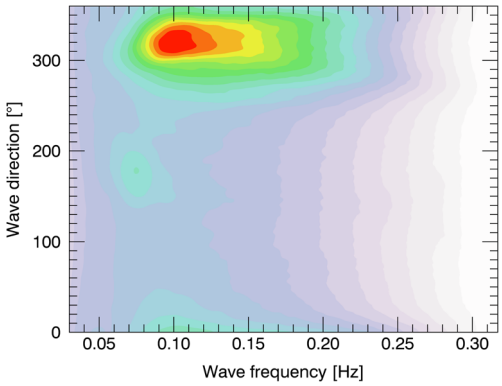

Fig. 19 Azimuthally-averaged frequency-direction spectrum on a logarithmic *white-to-red color scale* for mid-range (1-h mean, $t = 5.5$ h)

already observed in the literature (e.g. Hwang and Wang 2001), the spectrum shows evidence of bimodality at higher frequencies.

Figure 20 gives the MR and Datawell wave power, mean direction, and directional spreading as functions of frequency for the 1-h period around $t = 5.5$ h. The raw buoy power spectrum in Fig. 20a (*dashed line*) is spiky, which is likely due to natural sampling variability. The *solid black line* shows the same data but smoothed over five frequency bins. Both data sets begin at a frequency of 0.03 s^{-1}. We chose to cut off the buoy record (which extends to 0.5 s^{-1}, with a frequency resolution of 0.05 s^{-1}) at ~ 0.32 s^{-1} to match the radar frequency range. The radar record includes estimates for the near, mid, and far range. As far as the power spectrum is concerned, the mid-range spectrum agrees best with the reference data, especially around the peak. The MR mean direction and directional spreading estimates shown in Fig. 20b are both in qualitatively good agreement with the Datawell measurement. However, starting from a frequency of ~ 0.15 s^{-1}, the directional spreading records from the two sensors begin to deviate significantly. Regarding the mean direction, both sensors show a clear low-frequency dip, which is more pronounced but also much spikier for the Datawell buoy. This dip is due to the southern swell signal we observed in Fig. 19. Regarding range, all three agree reasonably well on mean direction, however, the respective low-frequency dips take very different shapes. The range dependency is more pronounced for the spreading direction: Starting around the spectral peak of ~ 0.10 s^{-1}, the far-range spreading is $\sim$ 10° greater than the mid-range spreading, which in turn exceeds the near-range spreading by about 10°.

Figures 21 and 22 analyze the same mid-range MR and Datawell wave properties as functions of time, covering the first 6 h of our study period. The figures confirm the observations we made above for $t = 5.5$ h. The wave properties measured by both sensors are in good qualitative agreement. The most notable difference concerns the higher-frequency spreading direction which grows much faster for the MR than it does for the Datawell buoy. If we compare the MR and Datawell buoy directional spreading to measurements that have been reported in the literature (e.g., Ewans 1998, Fig. 4), we find that the truth may lie in the middle, with the MR overestimating and the Datawell buoy underestimating the actual spreading. Finally, to illustrate the Datawell power spectra's spikiness, we decided to show both the raw data and a 5-frequency-bin smoothed version.

To conclude our spectral comparisons, Fig. 23a shows the ratio between the mid-range MR and Datawell buoy frequency wave spectra for the first 6 h of our study period. These results were obtained by interpolating the buoy record to match the MR frequency resolution. We also scaled the radar spectra to exactly match the spectral density measured by the buoy in order to remove possibly sub-optimal

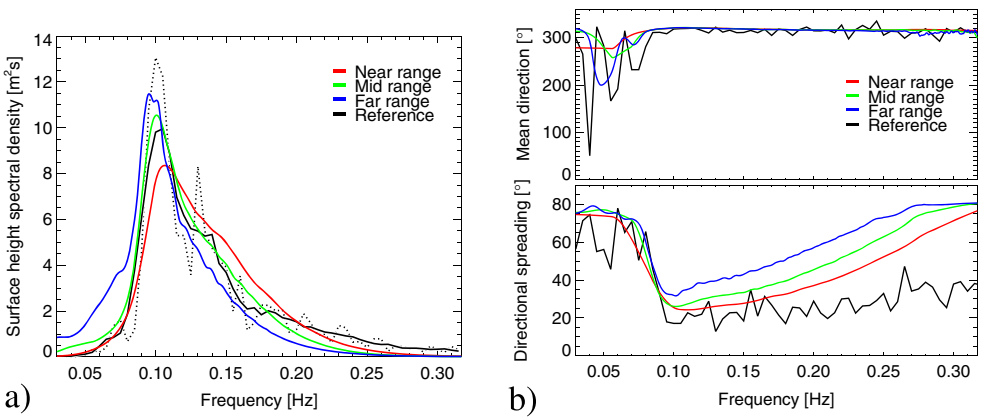

Fig. 20 **a** Frequency spectra for all three ranges and from Datawell buoy. The *dashed curve* corresponds to the raw Datawell data, the *solid black curve* shows the same data smoothed over five frequency bins. **b** Spreading and mean direction measurements by the Datawell buoy and the radar at all three ranges. Both **a**, **b** correspond to the 1-h period around $t = 5.5$ h

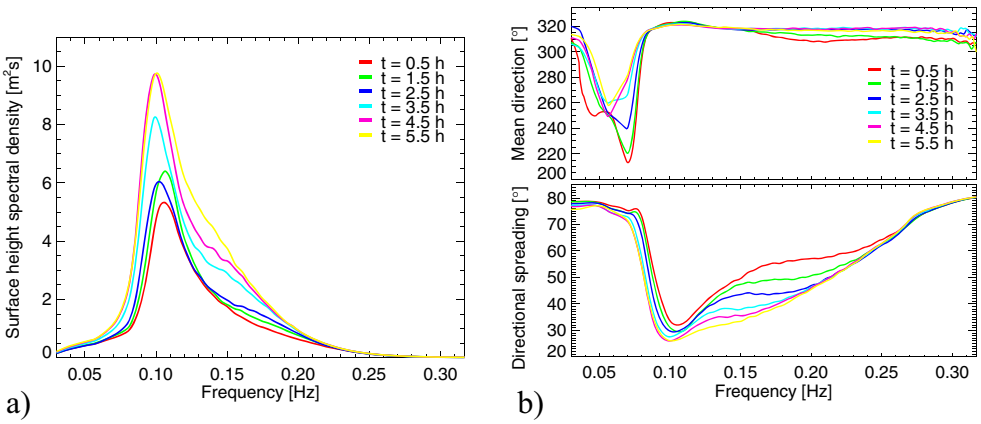

Fig. 21 **a** Radar-derived frequency wave spectra. **b** Spreading direction, and mean direction. *Curves* show 1-h averages of the mid-range results

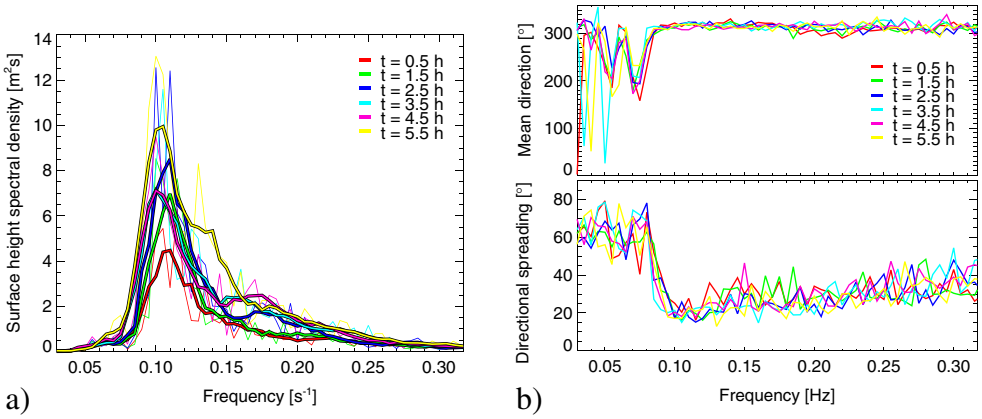

Fig. 22 **a** Frequency wave spectra measured by the Datawell buoy. The *thick lines* show the same data smoothed over five frequency bins. **b** Spreading and mean direction from the Datawell buoy. Both **a**, **b** cover the first 6 h of our study period

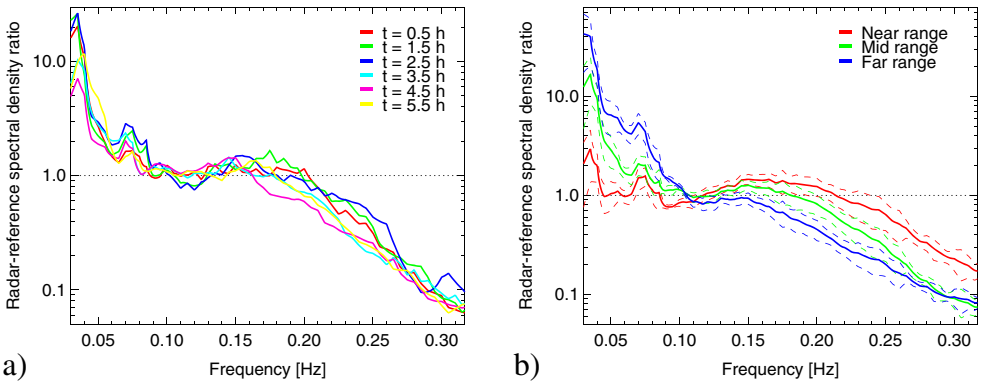

Fig. 23 **a** Ratios between mid-range radar and Datawell frequency wave spectra for first 6 h of study period. **b** Mean ratios for all ranges, averaged over same 6-h period, with *dashed lines* marking one standard deviation above and below the mean

radar-H_s calibration constants as a source of differences. For the same period, the mean ratios together with the corresponding standard deviations are shown in Fig. 23b. Note the logarithmic scale for the y-axis in both graphs. Assuming that the buoy record represents the true sea state, the figure shows that the radar consistently overestimates the low-frequency and underestimates the high-frequency power by up to an order of magnitude in either sense. However, it is encouraging that both sensors tend to agree well in the frequency range where most of the wave energy is concentrated, i.e., from 0.08 to 0.20 s^{-1}. What is more, the consistent nature of this bias in a growing sea state suggests that it could easily be corrected for, e.g., by dividing the radar frequency spectra by a smoothed version of the averaged ratios we show here. Regarding the different MR ranges, it is noteworthy that the mid-range record shows the best agreement around the peak of the spectrum, while the near-range estimate performs better at the low- and high-frequency ends.

5 Conclusions and outlook

As a surface wave monitoring instrument, MR has, in principle, several advantages over traditional heave-pitch-roll buoys. Firstly, in contrast to single-point-triplets, MRs are capable of sampling the fully-directional 2D wave spectrum, enabling them to pick up multimodal seas. Secondly, MRs measure waves at a high spatio-temporal resolution, making it possible to document sea state changes on short time scales or investigate the wave field's spatial variability. Thirdly, in addition to wave estimates, they may yield valuable information on surface currents and bathymetry as a by-product. Finally, MR wave monitoring has great potential on ocean-going vessels, where reliable wave measurements are very difficult to obtain and navigational radars are already near ubiquitous. In view of all these advantages, it appears surprising why MR has not gained greater traction as a surface wave sensor. We believe that the negligence of the range-azimuth dependency by the available commercial systems will increase the errors associated with their wave estimates, especially for shipboard stations, which may be part of the reason why they have failed to find more widespread use.

This study has clearly demonstrated that MR surface wave spectra and peak wave parameters exhibit a strong dependency on analysis window range and azimuth. This dependency was most marked for the signal-to-noise ratio SNR, used to determine the significant wave height H_s, which other investigators who used shipboard MR data have found to be the most lacking (e.g., Cifuentes-Lorenzen et al. 2013). For the most common case, where a segment of the radar FOV is blocked, we propose a least-squares regression method to determine the values for the up- and/or downwave SNR peak. Here, we determined calibration constants for both SNR peaks using H_s measurements from a Datawell buoy. This technique would allow us to reliably determine H_s even if the radar FOV covered only 180°. In the rare case of an unobstructed 360°-wide FOV, best results can be expected from simply averaging wave spectra or bulk parameters over all directions. Regarding the peak wave period T_p and peak wave direction θ_p, we found a 180°-symmetry in both parameters' azimuth dependencies. To correct for these dependencies, we therefore propose to average over results retrieved from analysis windows that cover either 180° or (if possible) 360° of the radar FOV. Regarding the range dependency, our peak wave parameter and spectral comparisons with the Datawell reference measurements indicate that best results can be expected from analysis windows at a mid-range location.

An area for future work concerns the MR surface current estimates. The surface current is determined from the Doppler shift of the surface wave coordinates within the 3D radar image spectrum (refer to Section 3 for details). As shown by Stewart and Joy (1974), the radar-based surface currents correspond to the average current from the surface to a depth of the order of $(2k)^{-1}$, where k is the wave number of the sampled ocean wave. Assuming a wind-driven current with a logarithmic profile, long waves should experience a smaller Doppler shift than short waves. The mean depth at which a MR samples the surface current thus depends on the wave number coordinates chosen for the current fit. While we found that our surface current estimates agree reasonably well over all ranges and azimuths, we are currently investigating whether the remaining variability may be explained by the fact that the spectral coordinates that were fed into the current fit algorithm vary significantly between analysis windows.

Finally, we would like to reiterate a point already made by Senet et al. (2001). To accurately measure surface waves and other oceanographic phenomena, we need to improve our understanding of the shape of the background noise (and the group line) within the 3D radar image spectrum. As part of our current research, we are developing a technique to parameterize the background noise's shape. We hope that these efforts will help further improve MR oceanographic products.

References

Alpers WR, Hasselmann K (1982) Spectral signal to clutter and thermal noise properties of ocean wave imaging synthetic aperture radars. Int J Remote Sens 3(4):423–446

Alpers WR, Ross DB, Rufenach CL (1981) On the detectability of ocean surface waves by real and synthetic aperture radar. J Geophys Res 86(C7):6481–6498

Bell PS (1999) Shallow water bathymetry derived from an analysis of X-band marine radar images of waves. Coast Eng 37(3-4):513–527

Bell PS, Osler JC (2011) Mapping bathymetry using X-band marine radar data recorded from a moving vessel. Ocean Dyn 61(12):2141–2156

Borge JCN, Soares CG (2000) Analysis of directional wave fields using X-band navigation radar. Coast Eng 40(4):375–391

Borge JCN, Reichert K, Dittmer J (1999) Use of nautical radar as a wave monitoring instrument. Coast Eng 37(3-4):331–342

Borge JCN, Rodríguez Rodríquez G, Hessner K, González PI (2004) Inversion of marine radar images for surface wave analysis. J Atmos Oceanic Technol 21(8):1291–1300

Borge JCN, Hessner K, Jarabo-Amores P, de la Mata-Moya D (2008) Signal-to-noise ratio analysis to estimate ocean wave heights from X-band marine radar image time series. IET Radar Sonar Navig 2(1):35–41

Catalán PA, Haller MC, Holman RA, Plant WJ (2011) Optical and microwave detection of wave breaking in the surf zone. IEEE Trans Geosci Remote Sens 49(6 Part 1):1879–1893

Cifuentes-Lorenzen A, Edson JB, Zappa CJ, Bariteau L (2013) A multisensor comparison of ocean wave frequency spectra from a research vessel during the Southern Ocean Gas exchange experiment. J Atmos Oceanic Technol

Collins CO, Lund B, Ramos RJ, Drennan WM, Graber HC (2013) Multi-platform wave parameter inter-comparison and evaluation during the ITOP experiment. J Atmos Oceanic Technol

COST Action 714 (2005) Measuring and analysing the directional spectrum of ocean waves. Office for Official Publications of the European Communities

Croney J (1966) Improved radar visibility of small targets in sea clutter. Radio Electron Eng 32(3):135–147

Dankert H, Horstmann J (2007) A marine radar wind sensor. J Atmos Oceanic Technol 24(9):1629–1642

Donelan MA, Drennan WM, Katsaros KB (1997) The air-sea momentum flux in conditions of wind sea and swell. J Phys Oceanogr 27(10):2087–2099

Ewans KC (1998) Observations of the directional spectrum of fetch-limited waves. J Phys Oceanogr 28(3):495–512

Frasier SJ, McIntosh RE (1996) Observed wavenumber-frequency properties of microwave backscatter from the ocean surface at near-grazing angles. J Geophys Res C: Oceans 101(C8):18,391–18,407

Gommenginger CP, Ward NP, Fisher GJ, Robinson IS, Boxall SR (2000) Quantitative microwave backscatter measurements from the ocean surface using digital marine radar images. J Atmos Oceanic Technol 17(5):665–678

Hatten H, Seemann J, Horstmann J, Ziemer F (1998) Azimuthal dependence of the radar cross section and the spectral background noise of a nautical radar at grazing incidence. In: Proc. Geoscience and Remote Sensing Symposium, IEEE International, vol 5, pp 2490–2492

Hessner K, Hanson JL (2010) Extraction of coastal wavefield properties from X-band radar. In: Geoscience and remote sensing symposium. IEEE International, pp 4326–4329

Hessner K, Reichert K, Dittmer J, Borge J, Günther H (2001) Evaluation of WaMoS II wave data. In: Proc. fourth int. Symp. on ocean wave measurements and analysis:221–230

Hessner KG, Nieto-Borge JC, Bell PS (2008) Nautical radar measurements in Europe: applications of WaMoS II as a sensor for sea state, current and bathymetry. In: Remote sensing of the european seas. Springer, pp 435–446

Hwang PA, Wang DW (2001) Directional distributions and mean square slopes in the equilibrium and saturation ranges of the wave spectrum. J Phys Oceanogr 31(5):1346–1360

Komen GJ, Cavaleri L, Donelan M, Hasselmann K, Hasselmann S, Janssen P (1996) Dynamics and modelling of ocean waves. Cambridge University Press

Kuik AJ, van Vledder GP, Holthuijsen LH (1988) A method for the routine analysis of pitch-and-roll buoy wave data. J Phys Oceanogr 18(7):1020–1034

Lee PHY, Barter JD, Beach KL, Hindman CL, Lake BM, Rungaldier H, Shelton JC, Williams AB, Yee R, Yuen HC (1995) X band microwave backscattering from ocean waves. J Geophys Res 100(C2):2591–2611

Ludeno G, Orlandi A, Lugni C, Brandini C, Soldovieri F, Serafino F (2013) X-band marine radar system for high-speed navigation purposes: A test case on a cruise ship. IEEE Geosci Remote S PP(99):1–5

Lund B, Graber HC, Horstmann J (2012a) Ocean surface wind retrieval from stationary and moving platform marine radar data. In: Proc. Geoscience and remote sensing symposium, IEEE International, pp 2790–2793

Lund B, Graber HC, Romeiser R (2012b) Wind retrieval from ship-borne nautical X-band radar data. IEEE Trans Geosci Remote Sens 50(10):3800–3811

Lund B, Graber HC, Xue J, Romeiser R (2013) Analysis of internal wave signatures in marine radar data. IEEE Trans Geosci Remote Sens 51(9):4840–4852

Nielsen UD (2006) Estimations of on-site directional wave spectra from measured ship responses. Mar Struct 19(1):33–69

OceanWaveS GmbH (2012) WaMoS II, Wave Monitoring System, operating manual and installation guide

O'Reilly WC, Herbers THC, Seymour RJ, Guza RT (1996) A comparison of directional buoy and fixed platform measurements of Pacific swell. J Atmos Oceanic Technol 13(1):231–238

Plant W (1989) The modulation transfer function: Concept and applications. In: Komen G, Oost W (eds) Radar scattering from modulated wind waves: Proceedings of the workshop on modulation of short wind waves in the gravity-capillary range by non-uniform currents, Kluwer

Plant WJ, Keller WC (1990) Evidence of bragg scattering in microwave doppler spectra of sea return. J Geophys Res 95(C9):16,299–16,310

Ramos RJ, Lund B, Graber HC (2009) Determination of internal wave properties from X-band radar observations. Ocean Eng 36(14):1039–1047

Reichert K (1994) Analysis of the azimuth dependence of the navigation radar imaging of the sea surface (in German). Master's thesis, Universität Hamburg

Reichert K, Lund B (2007) Ground based remote sensing as a tool to measure spatial wave field variations in coastal approaches. J Coast Res, Proc 9th Int Coast Symp 50:427–431

Seemann J, Ziemer F, Senet CM (1997) A method for computing calibrated ocean wave spectra from measurements with a nautical X-band radar, pp 1148–1154

Senet CM, Seemann J, Ziemer F (2001) The near-surface current velocity determined from image sequences of the sea surface. IEEE Trans Geosci Remote Sens 39(3):492–505

Serafino F, Lugni C, Nieto Borge JC, Soldovieri F (2011) A simple strategy to mitigate the aliasing effect in X-band marine radar data: Numerical results for a 2d case. Sensors 11(1):1009–1027

Stewart RH, Joy JW (1974) HF radio measurements of surface currents. Deep-Sea Res Oceanogr Abstr 21(12):1039–1049

Stredulinsky DC, Thornhill EM (2011) Ship motion and wave radar data fusion for shipboard wave measurement. J Ship Res 55(2):73–85

Thomson J, D'Asaro EA, Cronin MF, Rogers WE, Harcourt RR, Shcherbina A (2013) Waves and the equilibrium range at ocean weather station P. J Geophys Res C: Oceans 118(11):5951–5962

Wetzel LB (1990) Surface waves and fluxes, Kluwer, chap electromagnetic scattering from the sea at low grazing angles, pp 109–171

Wyatt L, Green J, Gurgel KW, Nieto Borge J, Reichert K, Hessner K, Günther H, Rosenthal W, Saetra O, Reistad M (2003) Validation and intercomparisons of wave measurements and models during the euroROSE experiments. Coastal Eng 48(1):1–28

Young IR, Rosenthal W, Ziemer F (1985) A three-dimensional analysis of marine radar images for the determination of ocean wave directionality and surface currents. J Geophys Res 90(C1):1049–1059

Ziemer F (1995) An instrument for the survey of the directionality of the ocean wave field. In: Proc. WMO/IOC workshop on operational ocean monitoring using surface based radars, vol 32, pp 81–87

Ziemer F, Dittmer J (1994) A system to monitor ocean wave fields. In: Proc Oceans, IEEE, vol 2, pp 28–31